

**SUPPLEMENTAL FIGURE 1.** Conversion from DOI-specific  $w$  histograms to DOI histograms showing the DOI resolution of a single crystal at each depth. (A) Histograms of the DOI-estimation parameter  $w$  acquired at 2, 6, 10, 14 and 18 mm. (B) Fit between  $w$  and DOI via linear regression. (C) DOI histograms generated by taking the  $w$  histograms in (A) and multiplying by the slope of the linear fit in (B). (D) DOI resolution at each acquired depth based on the width of the Gaussians in (C).

## Supplemental Note 1. Sensitivity

Perhaps the most important parameter to consider when building a PET system is gamma ray detection sensitivity, which is directly related to signal-to-noise ratio (SNR) and thus determines patient throughput, delivered dose and image quality. Monte Carlo simulations using highly advanced software such as GATE are the most reliable way to model and calculate system-level sensitivity. However, relative improvements in sensitivity and comparisons between systems can be done analytically by calculating (a) geometric sensitivity and (b) sensitivity gain based on coincidence time resolution (CTR) for time-of-flight readout (TOF), which is equal to the SNR gain squared (1)

$$\Delta(SNR) = \sqrt{\frac{D}{\Delta x}}$$

$$\Delta(Sens) = \Delta(SNR)^2 = \frac{D}{\Delta x} \quad (1)$$

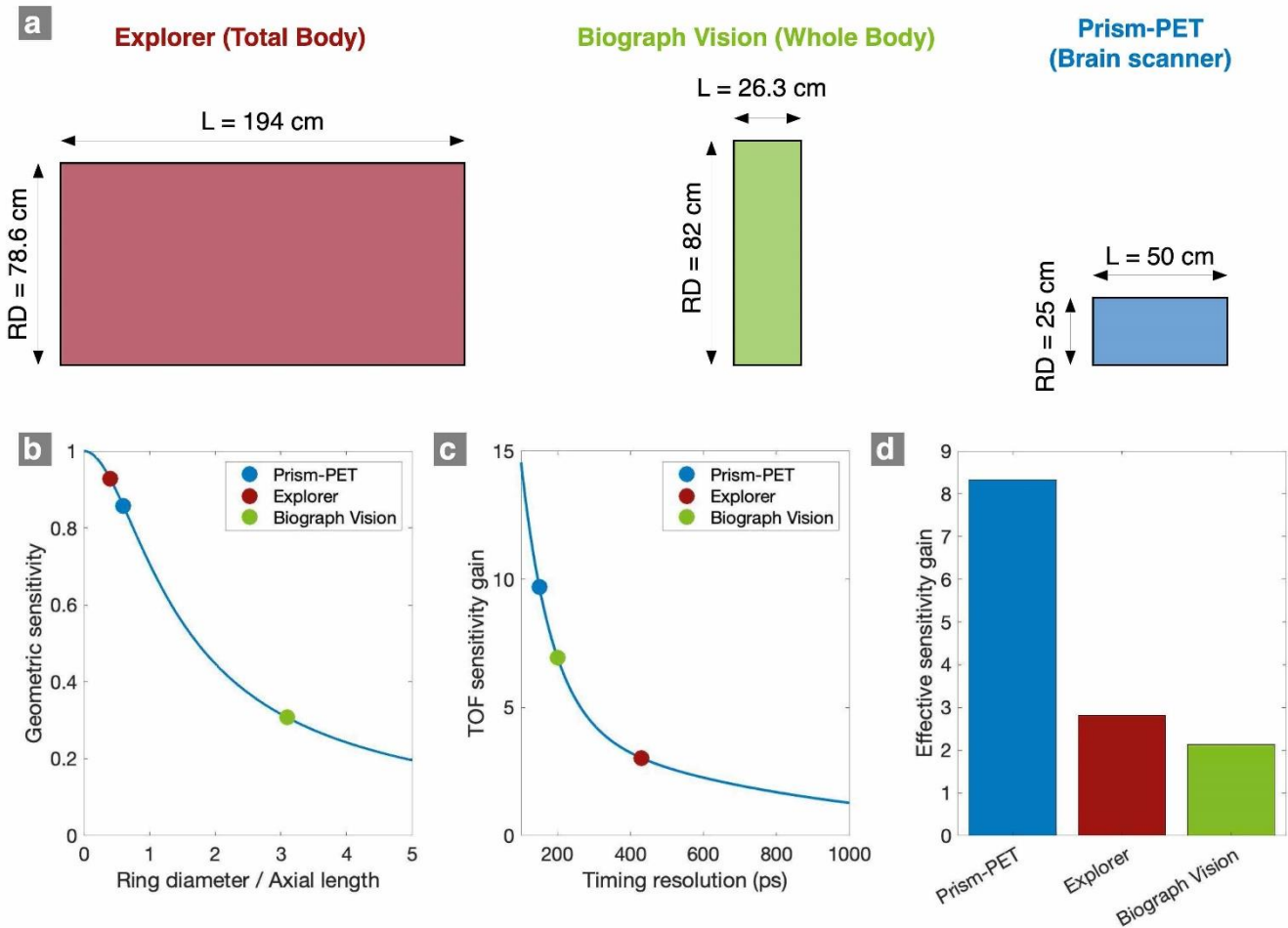
where  $D$  is the diameter of the object being imaged and  $\Delta x$  is the length of the reconstructed line segment along the line-of-response, which is directly proportional to the CTR ( $\Delta t$ ):

$$\Delta x = \frac{c * \Delta t}{2} \quad (2)$$

An example of a dedicated brain PET scanner that can be built with Prism-PET detector modules would be a cylindrical ring with 50 cm axial length and 25 cm diameter. Supplemental Fig. 2A shows the proposed brain Prism-PET scanner dimensions compared to those of an example whole-body (Siemens Biograph Visions) and total-body (EXPLORER) PET scanner. Having a small ring diameter and large axial field-of-view greatly improves the geometric efficiency (Supplemental Fig. 2B) at the cost of greatly increased parallax error and partial volume effect, which can be mitigated by performing depth-of-interaction (DOI) readout (2). As a result, small diameter organ-specific scanners should only be built with detector modules with DOI localization capabilities, such as our Prism-PET modules.

A recent paper demonstrated that DOI readout can also be used to recover CTR for TOF readout by deconvolving the DOI-dependence on coincidence timing (i.e., differences in path length in optical photons) (3). Assuming we have the same CTR reported in this paper ( $\sim 150$  ps), which is a safe lower bound estimate since our modules have better DOI resolution (2.5 mm vs. 3 mm), Prism-PET enables a TOF sensitivity gain close to a factor of 10 based on Eq. 1 when imaging an object with  $D \sim 20$  cm such as the human brain (Supplemental Fig. 2C). The TOF sensitivity gain for human brain imaging is slightly lower for Siemens Biograph Vision, which achieves  $\sim 220$  ps CTR (4), and much lower for the EXPLORER (Supplemental Fig. 2C), which has CTR  $> 400$  ps (5).

Supplemental Fig. 2D shows the overall effective sensitivity gain for human brain imaging when taking both geometric efficiency and TOF sensitivity gain into account. Based on our calculations, our proposed Prism-PET scanner may enable a three-fold and four-fold improvement in sensitivity compared to the Siemens Biograph Vision and EXPLORER scanners, respectively. However, experimental results are required to confirm Prism-PET's higher sensitivity via enhanced DOI-corrected CTR compared to the other state-of-the-art PET scanners.



**SUPPLEMENTAL FIGURE 2.** (A) Dimensions and geometric coverage of the Siemens Biograph Vision, EXPLORER Total-Body PET scanner, and an example of a Prism-PET brain scanner. (B) Geometric sensitivity for a point source positioned in the center of each of the scanners shown in (A). (C) Relative sensitivity gain as a function of coincidence timing resolution. (D) Effective sensitivity gain calculated as the product between geometric efficiency (as shown in (B)) and TOF sensitivity gain (as shown in (C)).

## Supplemental Note 2. Compton Localization

Prism-PET enables Compton scatter energy decomposition (and thus localization) due to its deterministic light sharing pattern. Let's assume we have a  $16 \times 16$  array of lutetium yttrium orthosilicate (LYSO) crystals with a Prism-PET light guide coupled 4-to-1 to an  $8 \times 8$  array of silicon photomultiplier (SiPM) pixels. We can approximate that each 511 keV gamma rays will produce a signal on 4 different pixels due to light sharing. The light sharing ratios between all crystals belonging to the same prismatoid can be measured directly using photoelectric events from flood data. Using this information, we can decompose the energies of the primary interaction (i.e., recoil electron) and secondary interaction site (i.e., scattered gamma ray). Once we have the decomposed energies, we can localize the two independently absorbed events in the scintillation blocks and determine the scattering angles and DOI. For the Prism-PET module, identifying a side-by-side Compton scattering event is possible because of the change from random light sharing for photoelectric events to a deterministic pattern (Supplemental Figs. 3 and 4).

Classical Compton energy decomposition can be performed as follows. The total absorbed energies  $E_A$  and  $E_B$  by the constituent elements A and B (scatter and recoil electron) are given as the summation of the energies in all 4 SiPMs

$$\begin{aligned} E_A &= \sum_{i=1}^4 E_{Ai} \\ E_B &= \sum_{i=1}^4 E_{Bi} \end{aligned} \quad (3)$$

where  $E_{A1}$  and  $E_{B1}$  are the maximum deposited energies in the SiPM coupled to the interacted crystal pixels and  $E_{A2,3,4}$  and  $E_{B2,3,4}$  are the deposited energies in the neighboring columns due to light leak at the bottom (from the SiPM side) and at the top via the prism-mirror light guide. The experimental results in Supplemental Fig. 3A illustrates the four known parameters  $E_{1-4}$  corresponding to the detected energies by each of the four pixels after the side-by-side Compton scattering event, where the total gamma particle energy deposited is

$$E_\gamma = E_A + E_B \quad (4)$$

Note that the energies of the constituent elements of the Compton scattering event, namely  $E_{A1-4}$  and  $E_{B1-4}$ , are unknown. Writing the equations based on the measured energies we obtain

$$\begin{aligned} E_1 &= E_{A1} + E_{B4} \\ E_2 &= E_{A2} + E_{B1} \\ E_3 &= E_{A3} + E_{B2} \\ E_4 &= E_{A4} + E_{B3} \end{aligned} \quad (5)$$

where we have 4 equations and 8 unknowns. However, the deposited energies in the neighboring columns are correlated. Let's consider the inset plot in Supplemental Fig. 3B where the maximum deposited energy occurred in the top-left SiPM. Given that the sharing fraction with the 3 neighbors depends on their proximity to the interacted crystal, and using the Pythagorean theorem by forming a right triangle using centers of the 3 neighbors as its vertices, we arrive at

$$\begin{aligned} \epsilon_{24} = d_{12}/d_{14} = 1 &\xrightarrow{\text{thus}} E_{A4} = \epsilon_{24}E_{A2} = E_{A2} \\ \epsilon_{23} = d_{12}/d_{13} = 1/\sqrt{2} = 0.7 &\xrightarrow{\text{thus}} E_{A3} = \epsilon_{23}E_{A2} = 0.7E_{A2} \end{aligned} \quad (6)$$

where, for example,  $d_{12}$  is the distance between the centers of the primary SiPM 1 and neighboring SiPM 2. Substituting Eq. 6 in Eq. 5 we get

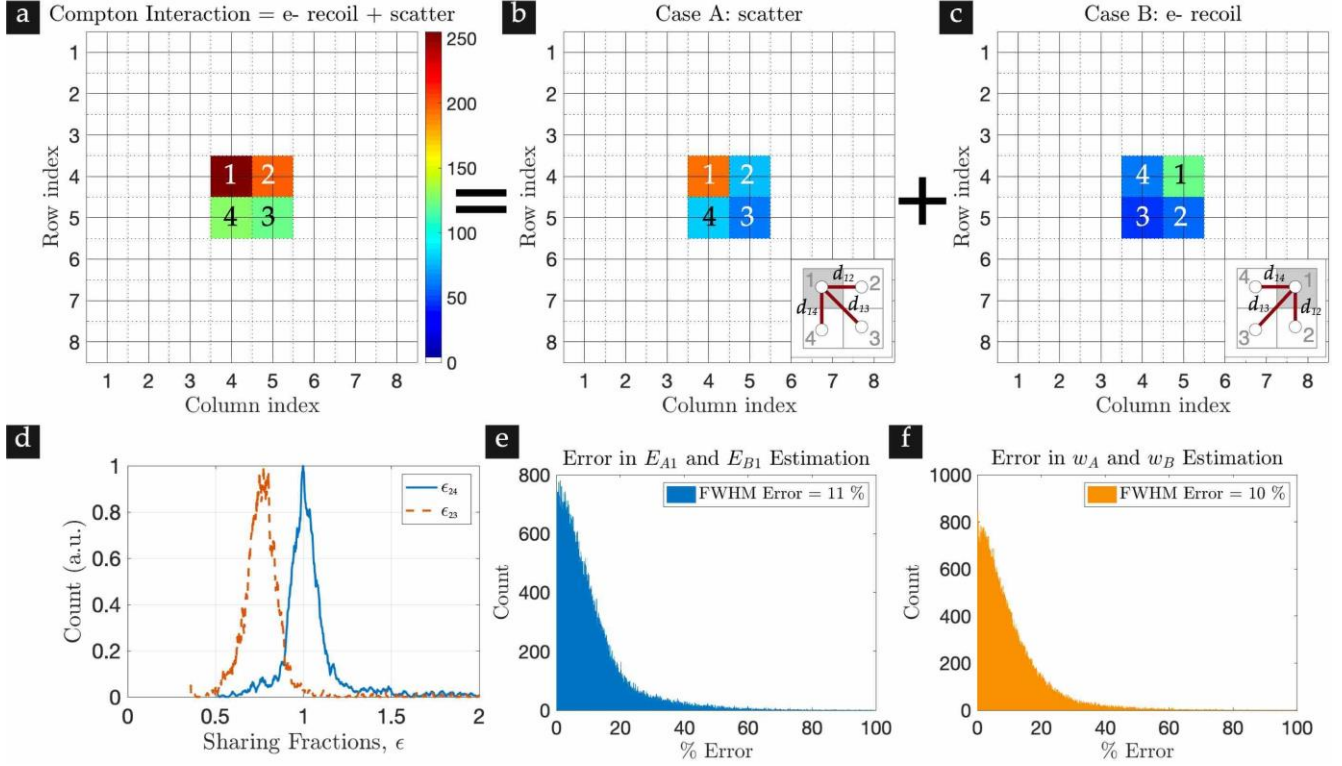
$$E_1 = E_{A1} + E_{B2}$$

$$E_2 = E_{A2} + E_{B1}$$

$$E_3 = 0.7E_{A2} + E_{B2}$$

$$E_4 = E_{A2} + 0.7E_{B2}$$

(7)



**SUPPLEMENTAL FIGURE 3.** (A)-(C) Example of Compton energy decomposition in a multicrystal scintillator array with Prism-PET. (D) Examples of light sharing fraction ratios between pixel 1 and neighboring pixels (as labeled in (A)-(C)). In one case (blue), both pixels (2 and 4) are adjacent to pixel 1 resulting in equal light sharing fractions, while in the other case (orange) pixel 3 is diagonally across from pixel 1 resulting in a smaller light sharing fraction. (E),(F) Energy and DOI error of Compton interaction decomposition for Prism-PET.

where we now have 4 equations and 4 unknowns. Note that in practice the sharing fractions will have spatial variations from the ideal cases shown in Eq. 6 due to some small and unavoidable misalignments between the prism-mirror light guides and the scintillator columns. However, as shown in Supplemental Fig. 3D, they can be obtained empirically across the array by analyzing the sharing fractions from individual photoelectric events obtained using the flood-histogram experiment. Supplemental Figs. 3B-C depict the two decomposed elements of a measured side-by-side Compton scattering event based on the above analysis.

Given that our modules have DOI localization, we can represent the DOI variables as

$$w_A = E_{A1}/E_A$$

$$w_B = E_{B1}/E_B$$

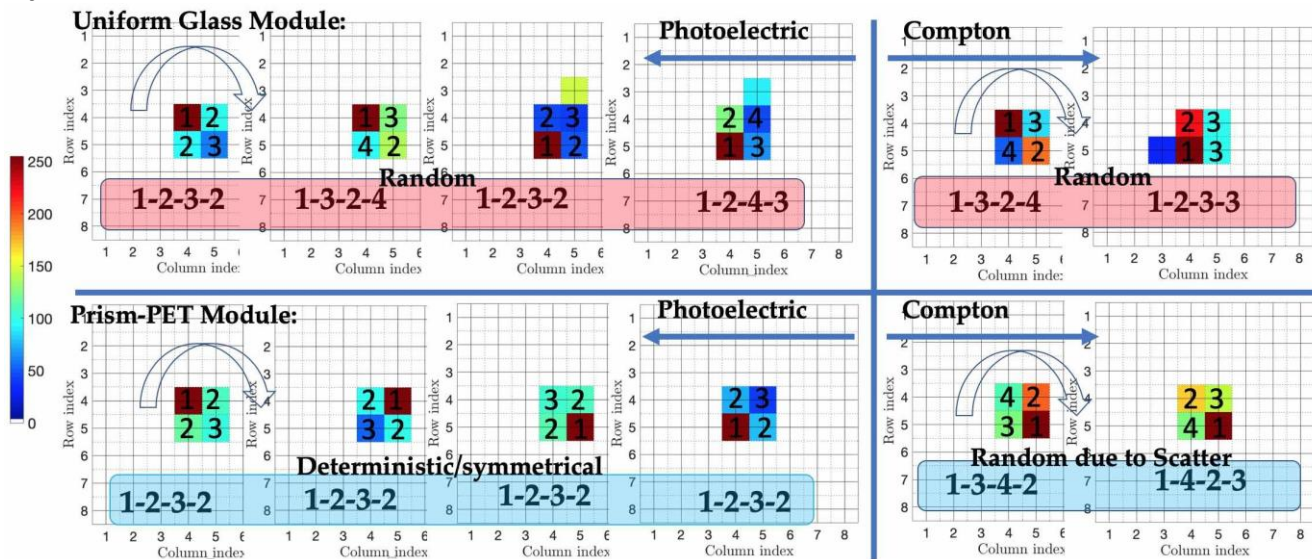
(8)

As shown in Supplemental Figs. 3E-F, the percent error for our estimation of  $\{E_{A1}, E_{B1}\}$  and  $\{w_A, w_B\}$  based on 200,000 experimental Gamma events is  $\sim 10\%$ . The error can be further reduced using

convolutional neural networks as the estimator specially since we can collect millions of Gamma events as training dataset using the flood-histogram experiment.

An example of how a Compton event where the recoil electron and scattered  $\gamma$ -ray are fully absorbed in adjacent scintillators in two different SiPMs can be decomposed into its constituent elements can be seen in Supplemental Fig. 3. Calculating the DOI variable  $w$  using classical Compton decomposition resulted in 11% full width at half maximum (FWHM) error (Supplemental Fig. 3E). In addition, Compton decomposition results in 15% FWHM energy error (Supplemental Fig. 3F).

Experimental results showing several examples of Compton events absorbed in adjacent crystals in a Prism-PET module vs. a module with a flat glass light guide can be seen in Supplemental Fig. 4. The light sharing pattern in the glass light guide module is random, making it difficult (and in most cases, impossible) to decompose the detected energies into the constituent energies of the scattered photon and recoil electron. Due to the right triangular prism geometry, the light sharing pattern is deterministic in the Prism-PET module, making it practical to decompose the event into its constituent energies based on the known light sharing ratios between crystals.



**SUPPLEMENTAL FIGURE 4.** Random light sharing pattern of a glass light guide (top) vs. deterministic light sharing pattern of Prism-PET (bottom).

## References

- [1] Surti S. Update on time-of-flight PET imaging. *J Nucl Med.* 2015;56:98–105.
- [2] Gong K, Majewski S, Kinahan PE, et al. Designing a compact high performance brain PET scanner—simulation study. *Phys Med Biol.* 2016;61:3681–3697.
- [3] Pizzichemi M, Polesel A, Stringhini G, et al. On light sharing TOF-PET modules with 3 mm depth of interaction and 157 ps FWHM Coincidence Time Resolution. *Phys Med Biol.* 2019;64:155008.
- [4] Reddin JS, Scheuermann JS, Bharkhada D, et al. Performance Evaluation of the SiPM-based Siemens Biograph Vision PET/CT System. In: *Conference Record of the 2018 IEEE Nuclear Science Symposium and Medical Imaging Conference.* Sydney, AU: IEEE; 2018.
- [5] Badawi RD, Shi H, Hu P, et al. First human imaging studies with the explorer total-body PET scanner. *J Nucl Med.* 2019;60:299–303.